Charge-Carrier Dynamics, Mobilities, and Diffusion Lengths of 2D–3D Hybrid Butylammonium–Cesium–Formamidinium Lead Halide Perovskites

Leonardo R. V. Buizza, Timothy W. Crothers, Zhiping Wang, Jay B. Patel, Rebecca L. Milot, Henry J. Snaith, Michael B. Johnston, and Laura M. Herz*

Perovskite solar cells (PSCs) have improved dramatically over the past decade, increasing in efficiency and gradually overcoming hurdles of temperature- and humidity-induced instability. Materials that combine high charge-carrier lifetimes and mobilities, strong absorption, and good crystallinity of 3D perovskites with the hydrophobic properties of 2D perovskites have become particularly promising candidates for use in solar cells. In order to fully understand the optoelectronic properties of these 2D–3D hybrid systems, the hybrid perovskite $BA_x(FA_{0.83}Cs_{0.17})_{1-x}Pb(I_{0.6}Br_{0.4})_3$ is investigated across the composition range $0 \leq x \leq 0.8$. Small amounts of butylammonium (BA) are found that help to improve crystallinity and appear to passivate grain boundaries, thus reducing trap-mediated charge-carrier recombination and enhancing charge-carrier mobilities. Excessive amounts of BA lead to poor crystallinity and inhomogeneous film formation, greatly reducing effective charge-carrier mobility. For low amounts of BA, the benevolent effects of reduced recombination and enhanced mobilities lead to charge-carrier diffusion lengths up to 7.7 µm for $x = 0.167$. These measurements pave the way for highly efficient, highly stable PSCs and other optoelectronic devices based on 2D–3D hybrid materials.

1. Introduction

The impressive growth of the field of perovskite solar cells (PSCs) has occurred alongside vast increases in photovoltaic installations worldwide, with 97 GW of capacity growth in 2017, a 26% increase on the previous year.[1] The use of metal halide perovskites (MHPs), which have an ABX_3 stoichiometry, as absorber materials has evolved rapidly since the initial use of perovskites nanocrystals as a sensitizer material for dye-sensitized solar cells (DSSCs) in 2009 by Miyasaka et al.[2] The two most commonly implemented solar cell structures to date are based on either the use of mesoporous electron-extracting metal oxides, with which the perovskite material is interspersed throughout; or the implementation of a planar heterojunction structure where the perovskite absorber layer lies in-between electron- and hole-extracting layers. Power conversion efficiencies (PCEs) based on such device architectures now exceed 23%[2–4] meaning that the focus has increasingly shifted to issues such as long-term stability.

Currently, the highest-performing MHPs incorporate a methylammonium (MA), formamidinium (FA) or cesium cation, or mixture thereof, at the A-site, lead or tin at the B-site and iodide or an iodide-bromide mixture as the anion at the X-sites. Typically, MHPs have strong optical absorption,[5] tunable bandgaps in the required regions for either single-junction or tandem solar cells,[6] high electron and hole mobilities,[7] a broad range of compositional tuning and are easily processable, usually via spin-coating of precursor solutions or the evaporation of precursors in a vacuum chamber.[8,9] The most commonly investigated MHP, MAPbI$_3$, has been shown to exhibit favorable properties for optoelectronic use,[5] including shallow trap states,[10,11] low Urbach energies,[12] and small phonon energies,[13,14] demonstrating the benign crystal structure of MHPs. Notwithstanding these impressive characteristics, MHP-based solar cells still struggle with stable performance over hundreds to thousands of hours, degrading due to interactions with light and moisture, as well as suffering from thermal instability and light-induced ion migration effects.[15–17] Attempts at altering the A-site cation by replacing MA with FA, cesium, or their mixtures have led to improved thermal stability and performance of solar cells.[18–20]

A recent innovative step towards materials with higher environmental stability has been the inclusion of 2D Ruddlesden–Popper phases inside the perovskite films. Here,

L. R. V. Buizza, T. W. Crothers, Dr. Z. Wang, Dr. J. B. Patel,
Prof. H. J. Snaith, Prof. M. B. Johnston, Prof. L. M. Herz
Clarendon Laboratory
Oxford University
Parks Road, OX1 3PU Oxford, UK
E-mail: laura.herz@physics.ox.ac.uk
Dr. R. L. Milot
Department of Physics
University of Warwick
Gibbet Hill Road, CV4 7AL Coventry, UK

the addition of larger, hydrophobic organic cations, such as 2-phenylethylammonium (PEA) or butylammonium (BA) to the precursors, leads to the formation of 2D layered structures, whose corner-sharing octahedral planes are separated by bilayers of monovalent organic cations that are too large to be directly incorporated into the ABX_3 perovskite crystal structure.[21,22] Fully layered Ruddlesden–Popper perovskites have a composition of the form $R_2A_{n-1}B_nX_{3n+1}$, where R is the larger organic cation and n determines the number of octahedral planes separated by the larger organic cations. For example, $n = 2$ would give two conjoined planes of corner-sharing octahedral, with the smaller A cations located between the octahedra and the larger R cations separating the octahedral planes. These 2D structures improve moisture-related stability substantially, producing devices that are stable over thousands of hours.[23,24] However, reduced light absorption and lower charge-carrier mobilities and diffusion lengths, especially in low-n materials, can lead to decreased PCEs for Ruddlesden–Popper perovskites, relative to their 3D counterparts.[25,26]

To address these drawbacks, the last two years have seen several attempts to combine the beneficial features of 2D and 3D perovskite structures through 2D–3D hybrid structures, which have yielded solar cells achieving high PCEs and excellent stability over thousands of hours.[27,28] One attempt at a hybrid structure involved a typical heterojunction device structure, combining $MAPbI_3$ with a Ruddlesden–Popper perovskite top layer that acts as a charge extraction layer and moisture barrier.[29] In another approach the combination of small amounts of aminovaleric acid iodide ($HOOC(CH_2)_4NH_3I$) with the usual MAI and PbI_2 precursors led to the formation of films comprising a thin layer of 2D perovskite, followed by a 2D–3D interface and then a bulk 3D phase.[27] In a third study, the substitution of mixed formamidinium–cesium with BA has been shown to result in a 3D bulk structure interspersed with smaller crystallites that contain a mixture of 2D Ruddlesden–Popper phases (i.e., with multiple n-values), referred to as a 2D–3D heterostructure.[28] In all of these cases, the formation of a 2D–3D hybrid structure leads to some alteration of optoelectronic properties, such as changes in photoluminescence (PL) intensity and peak position, as well as longer PL decay lifetimes. We emphasize the distinction between uniformly layered Ruddlesden–Popper systems with well-defined, low value of n, which exhibit relatively strong electronic and dielectric confinement, and such hybrid 2D–3D systems that involve a phase-segregated mixture of mainly 3D perovskite with some small amounts of 2D phase interspersed within or at the boundary of the 3D bulk. Such hybrid 2D–3D systems are targeting the best of both worlds—enhanced environmental stability of 2D Ruddlesden–Popper phases combined with the favorable electronic properties of 3D bulk MHPs.

To elucidate the influence of electronic confinement on optoelectronic properties, initial studies have investigated the charge-carrier dynamics in layered lead-halide perovskite Ruddlesden–Popper structures with varying n.[26,30] For such materials with low n values, confinement leads to the enhancement of excitonic peaks observed in absorption spectra and increases in monomolecular recombination rates as n decreases.[26] Further, transient absorption (TA) measurements display a broadening of spectral features with increasing value of n.[30]

In both cases, as n increases the optoelectronic behavior tends towards that of standard bulk 3D lead iodide perovskite. There has also been an initial reporting of TA measurements for 2D–3D heterostructures, with similar features observed for both 2D–3D materials and the associated pure 3D phase.[31] However, a systematic investigation of the impact of the 2D–3D hybrid structure on optoelectronic properties across a broad compositional range is still outstanding. Such work could clarify the compositional boundary at which hybrid 2D–3D systems approach the behavior of purely 3D perovskites, which is essential information for the successful implementation of these materials in photovoltaic devices. In particular, knowledge of trends in optoelectronic properties, especially charge-carrier recombination rate constants, mobilities, and diffusion lengths, will allow for an enhanced understanding of how best to tune these 2D–3D hybrid materials for optimized devices.

In this study, we present an investigation of charge-carrier dynamics, notably recombination rates and mobilities, for the system of 2D–3D hybrid perovskites $BA_x(FA_{0.83}Cs_{0.17})_{1-x}Pb(I_{0.6}Br_{0.4})_3$ with varying BA content ($0 \leq x \leq 0.8$). We find that the addition of small amounts of BA ($x < 0.2$) leads to enhanced crystallinity and lower monomolecular (trap-mediated) charge-carrier recombination rates, without having an adverse impact on the effective charge-carrier mobility. We suggest that the trend in monomolecular recombination rates is well explained by the formation of 2D crystallites within or surrounding the 3D bulk. These inclusions act to passivate grain boundaries and reduce trap state density, lowering the likelihood of trap-mediated recombination. Mono- and bimolecular recombination rates increase beyond $x = 0.33$, accompanied by a substantial drop-off in effective charge-carrier mobility. These trends are reflected in the charge-carrier diffusion lengths determined as a function of BA content, which exhibit an increase up to a peak value of 7.7 µm for $x = 0.167$, beyond which reduced charge-carrier mobilities and increased recombination rates lead to lower diffusion lengths for high BA content. Although bimolecular charge-carrier recombination rates are low throughout the composition range, we argue that the apparent increase in determined bimolecular rates observed for BA content $x \geq 0.5$ is caused by increased light outcoupling resulting from enhanced film roughness at high BA content. We find that excessive quantities of BA ($x \geq 0.5$) lead to poor morphological and compositional properties for photovoltaic devices, notably high charge-carrier recombination and low mobilities, and we thus define our boundary for 3D bulk-like behavior as $x < 0.5$, and ideally $x = 0.167$, for implementation of this 2D–3D hybrid perovskite system in photovoltaic devices.

2. Results and Discussion

2.1. Materials Synthesis and Film Preparation

Thin films of $BA_x(FA_{0.83}Cs_{0.17})_{1-x}Pb(I_{0.6}Br_{0.4})_3$ were prepared by the spin-coating of a blend of $FA_{0.83}Cs_{0.17}Pb(I_{0.6}Br_{0.4})_3$ and $BAPb(I_{0.6}Br_{0.4})_3$ precursor solutions (in N,N-dimethylformamide, DMF) onto z-cut quartz,[32] with the ratio of the two being varied such that the desired composition was achieved. All samples were dried in a nitrogen-filled glovebox on a hot plate at

70 °C for 60 s, followed by transfer into an oven where they were annealed in air at 175 °C for 80 min. Inclusion of BA in the films was verified through infrared absorption spectra which are able to track the fingerprint of a BA-specific C−N stretching mode near 1090 cm^{-1} (see Figure S2, Supporting Information). Full details of the sample preparation method are provided in the Supporting Information. We note that the method outlined above was optimized with the aim of achieving smooth films that incorporate a high density of 2D crystallites at the boundaries of 3D grains. This approach had previously been shown by us to result in the thin films containing plate-like 2D-phase crystallites standing up between 3D perovskite grains, as indicated by a combination of scanning electron microscopy images and 2D X-ray diffraction (XRD) measurements.[28] Crucially, for optimized stoichiometries such materials may be able to exhibit the advantageous combination of 3D-like charge transport and environmental stability, while also limiting pin-hole formation in devices that can arise from surface roughness, which we will explore here. In contrast to the methods typically employed to yield well-defined Ruddlesden–Popper phases, where increasing the value of n leads to more octahedral corner-sharing layers, the addition of BA in the manner employed here will ultimately lead to non-stoichiometries at very high BA composition. However, our experimental observations have shown that the alternative of addition of BA as part of Ruddlesden–Popper phases

in solution can lead to very high surface roughness. Thus, the method outlined here is optimized to strike a careful balance to yield a combination of optimized proportion and location of 2D crystallites, while also maintaining a smooth surface over a sufficiently large range of BA content.

2.2. Structural Changes Occurring with Increasing BA Content

Figure 1 shows the variation of several optoelectronic and crystallographic properties with BA content for thin films of BA$_x$(FA$_{0.83}$Cs$_{0.17}$)$_{1-x}$Pb(I$_{0.6}$Br$_{0.4}$)$_3$ (see Supporting Information for full experimental details). Figure 1A,B confirms that the addition of small amounts of BA greatly enhances the intensity of the (100) and (200) reflections in XRD measurements, and reduces any other (*hkl*) reflections (Figure 1A).[28] Similarly, the (200) reflection angle increases with BA content, and we observe the appearance of additional peaks, that are not present in the $x = 0$ spectrum, for compositions with $x \geq 0.333$ (see Figure 1B, and Figure S3E-I, Supporting Information). The enhanced intensity of the (100) and (200) peaks relative to other reflections is indicative of improved crystallinity throughout the film, with full-width half-maximum (FWHM) values lowest for $x = 0.167$ and rising beyond this to a value of FWHM = 0.25° for $x = 0.8$ (see Figure S4,
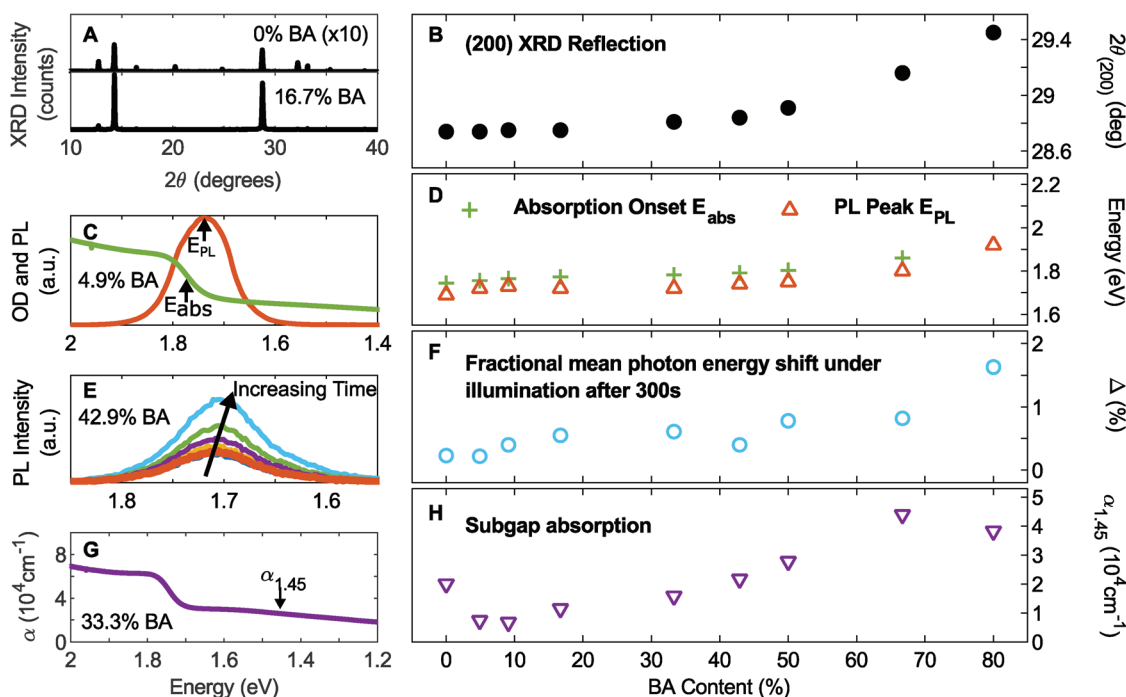

Figure 1. Variation of crystallographic and optoelectronic properties of BA$_x$(FA$_{0.83}$Cs$_{0.17}$)$_{1-x}$Pb(I$_{0.6}$Br$_{0.4}$)$_3$, for $x = 0$–0.8. A) XRD reflection patterns for $x = 0$ and 0.167. B) Shift in (200) reflection peak position, increasing monotonically as BA content increases. C) Absorption and PL spectra for $x = 0.049$. Absorption was measured using a Bruker Vertex 80v Fourier-Transform Infrared spectrometer, and PL was measured immediately following continuous wave excitation at 400 nm at 122 mWcm^{-2}. D) Absorption onset energy, calculated from the inflection point of the absorption spectrum, and PL peak emission energy. Both increase monotonically with BA content. E) PL spectra over time for $x = 0.429$. Samples were under sustained illumination using a continuous wave 400 nm beam at a fluence of 95 mWcm^{-2} and measured after 1, 10, 30, 60, 120, and 300 s. F) Percentage shift in mean photon energy over 300 s of continuous illumination, defined as parameter Δ (see the main text), for films that had been aged for three months under nitrogen atmosphere. For films with BA content of 0.67 and 0.8 significant spectral shifts had already occurred during aging, meaning that Δ could be even higher for unaged films. G) Absorption spectrum for $x = 0.333$, including below-bandgap scattering. H) Absorption coefficient at 1.45 eV, as a proxy for scattering from samples. Scattering is substantial above $x = 0.5$.

Supporting Information). The increase in (200) reflection angle with BA content has two potential explanations. As the BA content increases, the volume fraction of 2D crystallites increases, leading to additional strain on the 3D bulk, thus giving reduced interplanar spacing associated with larger reflection angles. Alternatively, these shifts with BA content could be caused by a variation in halide composition in the 3D bulk, with the iodide:bromide ratio changing from 60:40 towards closer to 50:50 in the bulk material. Such variation may result from a need for improved lattice matching at the 2D–3D grain boundaries with increased BA content. In this case, the higher measured reflection angles signify a decreased interatomic spacing resulting from the incorporation of a larger fraction of the smaller bromide anions in the 3D bulk. We discuss the distinction between these two mechanisms in more detail below.

2.3. Trends in Emission and Absorption with Increasing BA Content

Both the absorption onset and peak PL emission energy blueshift with increasing BA content (Figure 1D), with the $x = 0$ sample displaying an absorption onset at 1.74 eV (711 nm) and values increasing monotonically across the series, to 1.86 eV (667 nm) for $x = 0.667$. The change in PL and absorption spectra is continuous across the composition range, although for samples with very high BA content ($x = 0.667, 0.8$) it is clear that some inhomogeneity or phase-segregation is present, with a lack of clearly defined 3D bulk and 2D crystallite regions, as the absorption spectra are very broad and no longer exhibit clear onsets (see Figure S1, Supporting Information). Similar trends have been observed in 2D Ruddlesden–Popper systems, with both the absorption onset and PL peak blue-shifting with decreasing n-value.[26] However, we propose that the PL originates from the 3D bulk phase, rather than a confined Ruddlesden–Popper phase. This argument is supported by the lack of excitonic peaks that are typically observed in the absorption spectra of 2D systems. In addition, the absorption and PL spectra of our samples, even for high BA content, have very similar shapes to those of bulk 3D systems, in agreement with other reports on hybrid 2D–3D systems.[27,31] This observation, together with the inhomogeneity of the absorption spectra at high BA content, is the result of the way in which we have increased the BA content in the series, leading to an absence of clearer confinement effects at high BA content. However, we also note that given that all of the samples were very thick (>700 nm), it is also possible that additional features in the absorption spectra below 550 nm were not fully resolved due to low light transmission (Figure S1, Supporting Information).

The blueshift in bandgap that we observe via absorption and PL measurements with increasing BA content must also be correlated with the above-mentioned explanations for the corresponding increases in XRD reflection angles. The addition of BA to the materials under investigation here leads to lower interatomic spacing,[28] and if this were the only effect this might result in a corresponding decrease in the bandgap due to the positive deformation potential calculated for perovskites.[33,34] However, since the PL and absorption show a blueshift with increasing BA content we thus suggest that a convincing

explanation is that a slight variation in halide content exists within the 3D bulk region. The presence of a higher bromide fraction within the 3D bulk region of samples with a greater BA content will thus increase the bandgap whilst reducing the lattice spacing, which is consistent with the observed trends in both XRD peaks and bandgaps, as discussed in detail in the Supporting Information. We note that the Br-I content stated in the compositions reflects the halide composition in the starting solution; the final composition in the films after spin-coating and annealing may vary slightly from this ratio.

Accompanying these morphological changes is a broad feature in the absorption spectra below the bandgap (Figure 1G, H), which becomes significant at high BA contents. We attribute this subgap "absorption" (which is really a reduction in light transmission) to scattering caused by surface roughness. The lower scattering intensity observed for films with low BA content can be attributed to the improved crystal growth that is observed in the XRD data, leading to better grain alignment and thus giving smoother surfaces and lower light scattering at long wavelengths.

2.4. Material Aging and Stability Against light-Induced Halide Segregation

To investigate the long-term stability of the materials, we aged the thin films of $BA_x(FA_{0.83}Cs_{0.17})_{1-x}Pb(I_{0.6}Br_{0.4})_3$ for three months in an inert nitrogen glovebox (as an approximation of the effect of encapsulation for devices) and subsequently re-measured PL spectra to probe for any potential changes in halide distribution. Figure S1 in the Supporting Information shows the PL spectra as they were originally measured for freshly prepared samples (with extracted peak positions given in Figure 1D), while Figure S5 in the Supporting Information shows the PL spectra after the aging process. For all compositions, the spectra had shifted somewhat relative to the original PL spectra, indicating that some amount of halide segregation or redistribution in material morphology may have taken place. For samples with BA content $x \leq 0.5$, this shift is relatively small, on the order of tens of nanometers. However, the shift becomes significant for $x = 0.667, 0.8$ (see Figure S5H, I, Supporting Information), where the main peaks at 690 and 646 nm now only appear as a secondary peak/shoulder, with the dominant peak in the spectra now at much longer wavelengths (Figure S5H, I, Supporting Information). Thus, at these very high BA fractions the presence of excess BA decreases long-term material compositional stability, even when the samples are stored in an inert atmosphere. For lower BA fractions, however, materials are stable, in agreement with a recent study that demonstrated a clear enhancement of long-term solar cell performance stability when BA content of $x = 0.091$ was included in devices based on $BA_x(FA_{0.83}Cs_{0.17})_{1-x}Pb(I_{0.6}Br_{0.4})_3$, compared to BA-free ($x = 0$) devices.[28]

We further examined these aged films in terms of their stability against halide segregation under illumination. The issue of reversible light-induced shifts in PL spectra in lead mixed iodide–bromide perovskites has been known for a few years, and is commonly believed to derive from "halide segregation".[35] For example, the constant illumination of $MAPb(Br_yI_{1-y})_3$ films

with intermediate values of γ leads to the gradual appearance and growth of a lower energy secondary PL peak at $\approx$740 nm, which has been attributed to emission from an iodide-enriched phase. The proposed mechanism is that photoexcitation leads to the migration of halide ions, resulting in the phase segregation of the perovskite film into iodide- and bromide-rich regions.[16,35] This process has been shown to depend on the film crystallinity and morphology, bromide content γ, intensity of illumination, and the environment in which the film is illuminated, with studies suggesting a link with the propensity of the material to trap charge-carriers.[17,36,37] Modification of the A-cation site, e.g. by introduction of particular ratios of FA and cesium, has been shown to stabilize the material against photoinduced halide segregation by improving crystallinity.[36,38]

For our study, the aged $BA_x(FA_{0.83}Cs_{0.17})_{1-x}Pb(I_{0.6}Br_{0.4})_3$ films were excited using 400 nm continuous-wave illumination at 95 mWcm^{-2}, with PL spectra measured after 1, 10, 30, 60, 120, and 300 s. We find that for all samples the PL increases in intensity over time when under continuous illumination at approximately one-sun intensity, as has been previously observed in other mixed-halide systems (Figure S6, Supporting Information).[17,35] As a measure of the amount of halide segregation occurring we calculate the shift in mean photon energy of the PL spectra, E, relative to the initial mean photon energy, E_0, given by Δ:

$$\Delta = \frac{E_0 - E}{E_0}$$

For compositions with $x \leq 0.5$, the amount of segregation is negligible: Δ is less than one percent (Figure 1F). Such improved stability, relative to $MAPb(Br_yI_{1-y})_3$, observed here for $BA_x(FA_{0.83}Cs_{0.17})_{1-x}Pb(I_{0.6}Br_{0.4})_3$ with $x \leq 0.5$ is in good agreement with measurements of similar mixed-cation, mixed-halide systems,[19,36] in the absence of BA. For higher BA content ($x = 0.667$ and 0.8), the broad absorption spectra and significantly weaker XRD reflections measured for these samples indicate inhomogeneity and poor crystallinity of the films. Given the links between halide segregation and poor material crystallinity,[17,36,39,40] as well as high trap-mediated charge-carrier recombination (observed for samples with high BA content, as discussed further below), it is therefore not surprising that for $x = 0.667$ and 0.8, films not only show morphological changes with aging time, but also stronger PL spectral shifts Δ under illumination (Figure 1F).

Overall, the observed trends in the structural and optical properties of $BA_x(FA_{0.83}Cs_{0.17})_{1-x}Pb(I_{0.6}Br_{0.4})_3$ thin films illustrate the behavior of the hybrid 2D–3D system: for compositions up to $x = 0.5$, the materials behave analogously to typical 3D lead-halide perovskites, whilst for high quantities of BA ($x \geq 0.667$), there is increased inhomogeneity, poor crystal structure, low long-term stability, and increased halide segregation under illumination.

2.5. Trap-Mediated Charge-Carrier Recombination

We proceed to investigate charge-carrier dynamics (of freshly prepared films), first by measuring PL transient decays
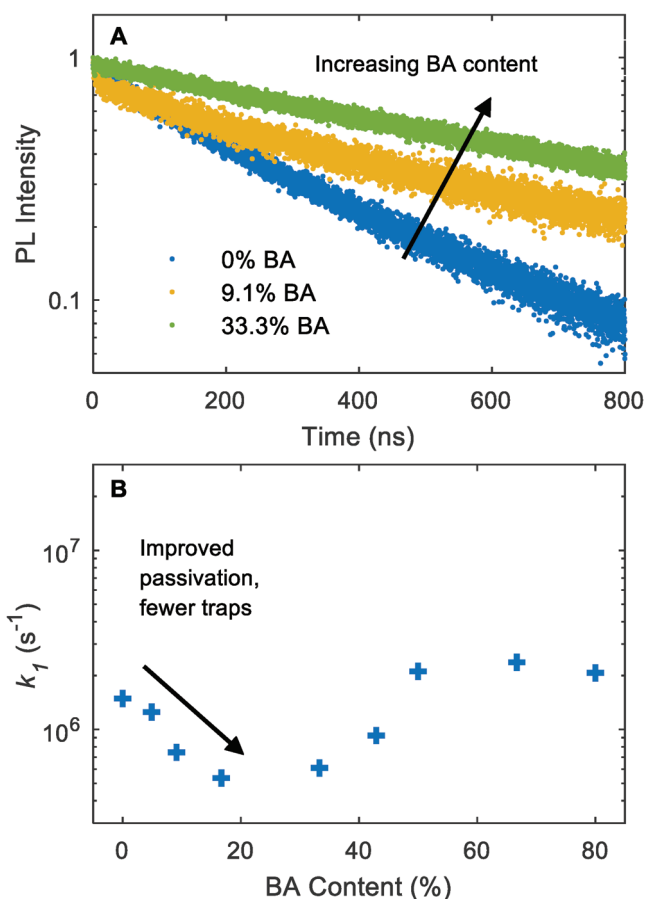

Figure 2. A) PL transients for three hybrid perovskite films of composition $BA_x(FA_{0.83}Cs_{0.17})_{1-x}Pb(I_{0.6}Br_{0.4})_3$ with $x = 0$, 0.091, and 0.333 (curves for further compositions and excitation fluences shown in the Supporting Information). Samples were measured by TCSPC, following pulsed excitation at 400 nm, with a 1 MHz repetition rate and a fluence of 4.4 nJ cm^{-2}. B) Monomolecular charge-carrier recombination rate (k_1) of $BA_x(FA_{0.83}Cs_{0.17})_{1-x}Pb(I_{0.6}Br_{0.4})_3$ across the composition range $x = 0$–0.8, determined by fitting monoexponential decays to PL decays (shown in Figure S7, Supporting Information).

using time-correlated single-photon counting (TCSPC, see Supporting Information for full experimental details). As has been shown across multiple perovskite compositions,[7,10,38,41–43] at the low excitation fluences employed, PL decays will mostly be dominated by trap-mediated (monomolecular) charge-carrier recombination. Previous reports for 2D–3D hybrid systems have noted that, relative to neat 3D systems, the introduction of large hydrophobic cations often reduces trap-mediated charge-carrier recombination.[27,28,31] For the $BA_x(FA_{0.83}Cs_{0.17})_{1-x}Pb(I_{0.6}Br_{0.4})_3$ thin films under investigation here, we find long PL decay lifetimes across the series of materials, on the order of hundreds of nanoseconds, whilst noting that the beneficial passivating characteristics of the hybrid systems begin to disappear above $x \geq 0.333$.

Figure 2 displays the impact of the addition of BA on monomolecular recombination rates for a select number of films (transients for all BA fractions and excitation fluences are provided in the Supporting Information). Films were photoexcited at an energy of 400 nm with fluences ranging from

**ADVANCED
SCIENCE NEWS**

www.advancedsciencenews.com

**ADVANCED
FUNCTIONAL
MATERIALS**

www.afm-journal.de

3 to 280 nJ cm^{-2}, and PL decays measured over 1000 ns. Figure 2A shows the highly monoexponential behavior of the PL transients at low excitation fluence—this trend is observed across all samples up to $x = 0.429$. Given that the instrument response function for our system is of the order of 150 ps, and in order to make a consistent comparison across the composition series, we fit a monoexponential expression to the transients taken at the lowest fluence, such that $I = I_0 \exp\left(-\dfrac{t}{\tau_1}\right)$. The fits begin at $t = 100$ ns, beyond which the decays are clearly monoexponential in the majority of compositions (Figure S7, Supporting Information). Because the radiative charge-carrier recombination component originates from band-to-band transitions,[44] we then take the monomolecular recombination rate of charge carriers to be $k_1 = \dfrac{1}{2\tau_1}$ (reflecting the proportionality of the PL intensity to $k_2 n^2$). We note that the factor of two is not always included in derivations of charge-carrier diffusion lengths derived from PL measurements, which should be kept in mind when values stated for charge-carrier recombination rates or diffusion lengths are compared across reports in the literature. The variation of k_1 with BA content composition is displayed in Figure 2B. We observe a clear passivating impact from the addition of BA, with lifetimes increasing substantially between $x = 0$–0.167, from $\tau_1 = 337$ to 935 ns (see Figure S7, Supporting Information). As we had recently shown through a combination of scanning electron microscopy images and 2D XRD measurements,[28] the material fabrication protocol employed here will lead to 2D perovskite crystallites accumulating at the boundary of large 3D perovskite grains. Therefore, the reduction in trap-mediated charge-carrier recombination rates at low BA content is most likely associated with the passivation of traps at the grain boundary, or the formation of an electronic barrier suppressing charge-carrier diffusion into traps.

Above the lower end of the composition range, we observe that the addition of BA leads to increased charge-carrier recombination, with rates rising to above 2×10^6 s^{-1} for $x \geq 0.5$. As has previously been reported, 2D Ruddlesden–Popper phase perovskites display highly excitonic recombination, especially for low n-values.[22,26] However, given the inhomogeneity, poor crystallinity and higher scattering of the films with high BA content, as well as the lack of any excitonic features in both the PL and absorption spectra in Figure S1 in the Supporting Information, it is likely that the observed increased in monomolecular recombination rates derive from a significant rise in the trap-state density for the fabrication procedure adopted here, rather than any excitonic effects.[45–47]

2.6. Bimolecular (band-to-band) Charge-Carrier Recombination

To assess the dependence of apparent band-to-band (bimolecular) charge-carrier recombination on the BA content in the materials, we measured photoconductivity transients at early times after excitation with elevated fluences, using the Optical-Pump Terahertz-Probe (OPTP) technique. The samples were excited at a wavelength of 400 nm through the front of the films,
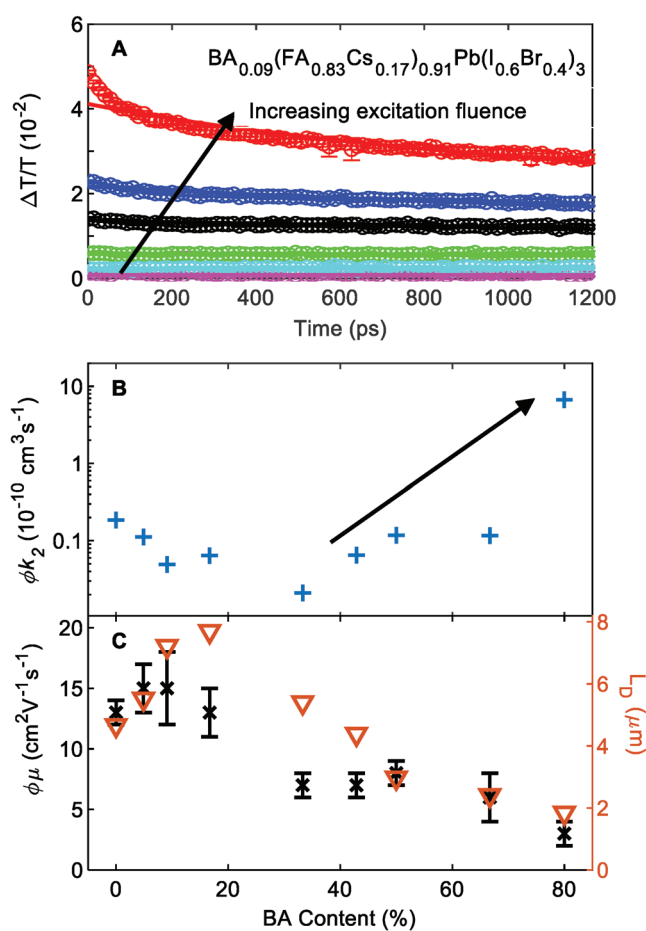

Figure 3. OPTP spectroscopy measurements for BA$_x$(FA$_{0.83}$Cs$_{0.17}$)$_{1-x}$Pb(I$_{0.6}$Br$_{0.4}$)$_3$ films using 400 nm pump. A) Example transient decays for excitation at fluences of 1.38, 4.8, 11.5, 26, 42, and 77 µJ cm^{-2} for a thin film of composition BA$_{0.09}$(FA$_{0.83}$Cs$_{0.17}$)$_{0.91}$Pb(I$_{0.6}$Br$_{0.4}$)$_3$ (curves for other compositions are shown in the Supporting Information). Data are given as open circles with error bars, and solid lines are fits according to Equation 2 (see the main text). B) Apparent bimolecular recombination rate (ϕk_2) across the composition range $x = 0$–0.8, extracted by fitting the OPTP transient decays. C) Values of the effective charge-carrier sum mobility $\phi \mu$ and diffusion length across the composition range. Diffusion length values are calculated at a charge-carrier density of $n = 10^{14}$ cm^{-3}.

and the fractional change in transmitted terahertz signal ($\Delta T/T$) was measured. Variation of the delay between the pump and probe beams allows for transient decays such as those shown in **Figure 3**A to be recorded. The initial $\Delta T/T$ signal can be converted into photoinduced conductivity, which is proportional to the product of charge-carrier density n and effective mobility $\phi \mu$ (see Supporting Information for further details). Hence, the initial value (immediately after photoexcitation) of the photoconductivity can be used to deduce the sum over the electron and hole mobilities in the material, if the density of initially created charge carriers is known (see Supporting Information). We note that the fraction of absorbed photons that is converted into free charge carriers, the photon-to-free-charge branching ratio ϕ, is not determined in this experiment. Thus, for clarity and consistency we present values in terms of the apparent bimolecular recombination rate constants ϕk_2 and

effective charge-carrier mobilities $\phi\mu$ (see Section H in the Supporting Information). For 3D lead halide perovskites $\phi = 1$ can be assumed, given that excitonic effects at room temperature are negligible as a result of the low exciton binding energy.[48] For Ruddlesden-Popper systems with low n-values, greater electronic confinement effects and larger exciton binding energies are present,[43] meaning that ϕ could potentially be smaller than one. In the 2D–3D hybrid system that we present here, 3D perovskite domains are interspersed with 2D crystallites near the grain boundaries,[28] and we might therefore expect the majority of photo-excited species to be free charge carriers. Terahertz photoconductivity spectra, presented in Figure S8 in the Supporting Information, indeed show a Drude-like free carrier response (positive flat real part, zero imaginary part, as expected for free carriers with short momentum relaxation time) across a range of compositions, indicating that the photoconductivity transients are dominated by the response of free charge carriers in these materials. Given that $0 \leq \phi \leq 1$, the presented values are thus underestimates of the true physical values.

The time dependence of the charge-carrier density n may be described by the following rate equation:

$$\frac{\partial n}{\partial t} = -k_3 n^3 - k_2 n^2 - k_1 n \tag{1}$$

where k_1 is the monomolecular recombination rate, k_2 is the bimolecular, and k_3 the Auger recombination rate constant. In order to separate out competing charge-carrier recombination mechanisms we use the solutions to this rate equation to carry out global fits to our data across multiple fluences, adjusting to account for the excitation density profile (see Supporting Information for details of the fitting, and Figure 3A and Figure S9, Supporting Information, for data and fits).[41,43,49] We find that typical values of k_3 near 2×10^{-29} cm^{6}s^{-1} mean that,[43,46] at the fluences we employ here, Auger recombination makes an insignificant contribution, and we therefore set k_3 to zero. In this case, we may use the following analytical solution to equation (1) to fit our data:

$$n(t) = \frac{k_1 \alpha}{e^{k_1 t} - \alpha k_2} \quad \text{for} \quad \frac{1}{\alpha} = \frac{k_1}{n_0} + k_2 \tag{2}$$

where n_0 is the initial amplitude of the transient decay (derivation given in the Supporting Information). Values of k_1 are fixed to those extracted from the TCSPC measurements that were taken over much longer time scales, but we note that given the measurement window of 1.2 ns for the photoconductivity transients, all of the monomolecular recombination lifetimes are too long to have any significant impact on the fit results. The dominant contribution therefore is from radiative bimolecular charge-carrier recombination. This process has been shown to be the inverse of photon absorption,[50] and is mediated by photon reabsorption, which masks the intrinsic recombination rates in a material, in particular for thicker films.[51]

Figure 3B shows the values extracted for the apparent bimolecular recombination rate constant as a function of BA content. For most films, ϕk_2 is close to 0.1×10^{-10} cm^{3}s^{-1}, similar to previously measured values for $(FA_{0.83}Cs_{0.17})Pb(I_{0.6}Br_{0.4})_3$,[36] however, samples with higher BA content appear to have higher

rate constants, rising up to 6.7×10^{-10} cm^{3}s^{-1}. The variability of bimolecular recombination rate constants reported for prototypical MAPbI$_3$ in the literature ($0.6 - 23 \times 10^{-10}$ cm^{3}s^{-1}) has been addressed in work by Crothers et al.,[51] who proposed that the re-absorption of emitted photons within a thin film may reduce the apparent, externally measured values of the bi-molecular charge-carrier recombination constants.[43,51] Since photon reabsorption will be affected by film thickness and light scattering, these effects can lead to a large variation of the determined values of k_2. Our samples were relatively thick (>700 nm), meaning that both photon reabsorption and charge-carrier diffusion will play a significant role. Hence, the apparent bimolecular recombination rate constants we determine here will be lower than the true intrinsic values expected from the principle of detailed balance.[50] We therefore attribute the rise in values of ϕk_2 with BA content to poorer photon retention and increased photon out-coupling from the thin films. Such increased outcoupling for higher BA content should be expected, given that we observe a reduction in the light transmitted through the films at photon energies below the bandgap (see Figure 1H, and Figure S1, Supporting Information), indicative of higher surface roughness that will scatter light near the emission energy of recombining charge carriers. Therefore, while for low BA content the films are smooth and have improved photon-retention capability, leading to the observed low values of ϕk_2,[51] at high BA content increased scattering and light outcoupling results in a higher value of 6.7×10^{-10} cm^{3}s^{-1} for $x = 0.8$, which is close to the intrinsic limit recently determined for MAPbI$_3$.[51]

2.7. Effective Charge-Carrier Mobility and Diffusion Lengths

Figure 3C displays the effective charge-carrier mobility values extracted from OPTP measurements for films of $BA_x(FA_{0.83}Cs_{0.17})_{1-x}Pb(I_{0.6}Br_{0.4})_3$, with values ranging from 13 to 15 cm^{2}V^{-1}s^{-1} for $x \leq 0.167$, which are well within the range required for efficient photovoltaic device performance.[49] However, as the BA content is further increased, charge-carrier mobilities rapidly decline down to 3 ± 1 cm^{2}V^{-1}s^{-1} for $BA_{0.8}(FA_{0.83}Cs_{0.17})_{0.2}Pb(I_{0.6}Br_{0.4})_3$ ($x = 0.8$). The measured value of 13 ± 2 cm^{2}V^{-1}s^{-1} for the BA-free $(FA_{0.83}Cs_{0.17})Pb(I_{0.6}Br_{0.4})_3$ is in excellent agreement with previously reported values.[36] While there have been reports of charge-carrier mobilities in Ruddlesden–Popper perovskite systems declining with decreasing number of layers n, as electronic confinement is increased,[26,52] the lack of sharp absorption features in the films with high BA content means that this explanation is unlikely to hold here. Instead, we propose that the decline in effective charge-carrier mobility for high BA content is associated with a deterioration in material crystallinity, as supported by the increase in the width and decrease in intensity of the XRD diffraction peaks (see Figures S3 and S4 in Supporting Information).

Finally, we combine the measured charge-carrier recombination constants and mobilities in order to extract charge-carrier diffusion lengths across the composition range, using the following equation:

$$L_D = \sqrt{\frac{D}{R_{tot}(n)}} = \sqrt{\frac{\mu k_B T}{e R_{tot}(n)}} \tag{3}$$

where the total charge-carrier recombination rate is $R_{tot} = -\frac{1}{n}\frac{dn}{dt} = nk_2 + k_1$, and we have taken $k_3 = 0$ as discussed above (meaning that the equation approximately holds for $n < 10^{16} \text{cm}^{-3}$). Because of the dependence of the charge-carrier recombination rate R_{tot} on the density of charge carriers n, the charge-carrier diffusion length itself will depend on the absorbed photon density. We calculate the diffusion lengths at a charge-carrier density of $\approx 10^{14} \text{ cm}^{-3}$, which is close to the expected density generated under AM1.5 solar irradiation for materials with monomolecular (trap-mediated) carrier lifetimes similar to those measured here.[49] We find charge-carrier diffusion lengths exceeding 1.8 µm across the composition range, with a maximum value of 7.7 µm for $BA_{0.17}(FA_{0.83}Cs_{0.17})_{0.83}Pb(I_{0.6}Br_{0.4})_3$. These values are well above the film thickness required in order for most of the light with photon energies above the bandgap to be absorbed, according to absorption depths of between 100 and 1000 nm across the above-gap solar spectrum (see Figure S1 in the Supporting Information). The peak in diffusion lengths at compositions with $x = 0.091$ and 0.167 correlates well with previous device studies that find excellent solar cell performance for low BA content, as well as other reports of improved device performance for low amounts of 2D–3D hybridization.[27,28,31] Our study therefore demonstrates that the reason for such excellent performance is the combination of a reduction in trap-mediated charge-carrier recombination coupled with maintained good effective charge-carrier mobility for low BA content.

3. Conclusions

In summary, we have investigated the optoelectronic properties of 2D–3D hybrid perovskites $BA_x(FA_{0.83}Cs_{0.17})_{1-x}Pb(I_{0.6}Br_{0.4})_3$ across a wide range of BA contents $x = 0–0.8$. We find markedly improved charge-carrier lifetimes with the addition of small amounts of BA, with trap-mediated recombination rates decreasing by a factor of three between compositions with $x = 0$ and 0.167. However, when excessive amounts of BA are added, film formation is inhomogeneous and of low crystallinity, resulting in enhanced trap state densities, worsened photon retention, and significantly lower charge-carrier mobilities. A sweet spot is demonstrated for the addition of small amounts of BA ($x = 0.091–0.167$) where enhanced crystallinity and passivation of trap states at grain boundaries lead to much longer monomolecular lifetimes, and slightly enhanced charge-carrier mobilities relative to the BA-free 3D perovskite $(FA_{0.83}Cs_{0.17})Pb(I_{0.6}Br_{0.4})_3$, yielding charge diffusion lengths in excess of 7 µm, comfortably beyond requirements for efficient thin-film solar cells. Thus for this range, the materials exhibit beneficial properties of both 3D and 2D materials, i.e., a combination of excellent charge transporting properties with enhanced stability, including stability toward light induced halide segregation. Our study thus provides an explanation, based on the underlying optoelectronic properties of the $BA_x(FA_{0.83}Cs_{0.17})_{1-x}Pb(I_{0.6}Br_{0.4})_3$ hybrid system, for the excellent performance of hybrid 2D–3D perovskite systems that enables the fabrication of efficient and highly stable photovoltaic solar cells.

Supporting Information

Supporting Information is available from the Wiley Online Library or from the author.

Conflict of Interest

The authors declare no conflict of interest.

[1] International Energy Agency, "Renewables 2018," can be found under https://www.iea.org/renewables2018/, **n.d**.

[2] A. Kojima, K. Teshima, Y. Shirai, T. Miyasaka, *J. Am. Chem. Soc.* **2009**, *131*, 6050.

[3] W. S. Yang, B. Park, E. H. Jung, N. J. Jeon, *Science* **2017**, *356*, 1376.

[4] NREL, "Best Research-Cell Efficiency Chart | Photovoltaic Research | NREL," can be found under https://www.nrel.gov/pv/cell-efficiency.html, **n.d**.

[5] M. A. Green, A. Ho-Baillie, H. J. Snaith, *Nat. Photonics* **2014**, *8*, 506.

[6] L. Protesescu, S. Yakunin, M. I. Bodnarchuk, F. Krieg, R. Caputo, C. H. Hendon, R. X. Yang, A. Walsh, M. V. Kovalenko, *Nano Lett.* **2015**, *15*, 3692.

[7] C. Wehrenfennig, G. E. Eperon, M. B. Johnston, H. J. Snaith, L. M. Herz, *Adv. Mater.* **2014**, *26*, 1584.

[8] H. S. Kim, C. R. Lee, J. H. Im, K. B. Lee, T. Moehl, A. Marchioro, S. J. Moon, R. Humphry-Baker, J. H. Yum, J. E. Moser, M. Grätzel, N. G. Park, *Sci. Rep.* **2012**, *2*, 591.

[9] M. Liu, M. B. Johnston, H. J. Snaith, *Nature* **2013**, *501*, 395.

[10] D. W. deQuilettes, S. M. Vorpahl, S. D. Stranks, H. Nagaoka, G. E. Eperon, M. E. Ziffer, H. J. Snaith, D. S. Ginger, *Science* **2015**, *348*, 683.

[11] S. De Wolf, J. Holovsky, S.-J. Moon, P. Löper, B. Niesen, M. Ledinsky, F.-J. Haug, J.-H. Yum, C. Ballif, *J. Phys. Chem. Lett.* **2014**, *5*, 1035.

[12] A. Sadhanala, F. Deschler, T. H. Thomas, S. E. Dutton, K. C. Goedel, F. C. Hanusch, M. L. Lai, U. Steiner, T. Bein, P. Docampo, D. Cahen, R. H. Friend, *J. Phys. Chem. Lett.* **2014**, *5*, 2501.

[13] A. D. Wright, C. Verdi, R. L. Milot, G. E. Eperon, M. A. Pérez-Osorio, H. J. Snaith, F. Giustino, M. B. Johnston, L. M. Herz, *Nat. Commun.* **2016**, *7*, 11755.

[14] T. Kirchartz, T. Markvart, U. Rau, D. A. Egger, **2018**, *9*, 939.

[15] B. Conings, J. Drijkoningen, N. Gauquelin, A. Babayigit, J. D'Haen, L. D'Olieslaeger, A. Ethirajan, J. Verbeeck, J. Manca, E. Mosconi, F. De Angelis, H. G. Boyen, *Adv. Energy Mater.* **2015**, *5*, 1500477.

[16] D. J. Slotcavage, H. I. Karunadasa, M. D. McGehee, *ACS Energy Lett.* **2016**, *1*, 1199.

[17] A. J. Knight, A. D. Wright, J. B. Patel, D. P. McMeekin, H. J. Snaith, M. B. Johnston, L. M. Herz, *ACS Energy Lett.* **2019**, *4*, 75.

[18] G. E. Eperon, S. D. Stranks, C. Menelaou, M. B. Johnston, L. M. Herz, H. J. Snaith, *Energy Environ. Sci.* **2014**, *7*, 982.

[19] D. P. McMeekin, G. Sadoughi, W. Rehman, G. E. Eperon, M. Saliba, M. T. Horantner, A. Haghighirad, N. Sakai, L. Korte, B. Rech, M. B. Johnston, L. M. Herz, H. J. Snaith, *Science* **2016**, *351*, 151.

[20] C. Yi, J. Luo, S. Meloni, A. Boziki, N. Ashari-Astani, C. Grätzel, S. M. Zakeeruddin, U. Röthlisberger, M. Grätzel, *Energy Environ. Sci.* **2016**, *9*, 656.

[21] D. B. Mitzi, K. Chondroudis, C. R. Kagan, *IBM J. Res. Dev.* **2001**, *45*, 29.

[22] T. Ishihara, J. Takahashi, T. Goto, *Phys. Rev. B* **1990**, *42*, 11099.

[23] K. Yao, X. Wang, Y. Xu, F. Li, L. Zhou, *Chem. Mater.* **2016**, *28*, 3131.

[24] H. Tsai, W. Nie, J.-C. Blancon, C. C. Stoumpos, R. Asadpour, B. Harutyunyan, A. J. Neukirch, R. Verduzco, J. J. Crochet, S. Tretiak, L. Pedesseau, J. Even, M. A. Alam, G. Gupta, J. Lou, P. M. Ajayan, M. J. Bedzyk, M. G. Kanatzidis, A. D. Mohite, *Nature* **2016**, *536*, 312.

[25] C. C. Stoumpos, D. H. Cao, D. J. Clark, J. Young, J. M. Rondinelli, J. I. Jang, J. T. Hupp, M. G. Kanatzidis, *Chem. Mater.* **2016**, *28*, 2852.

[26] R. L. Milot, R. J. Sutton, G. E. Eperon, A. A. Haghighirad, J. Martinez Hardigree, L. Miranda, H. J. Snaith, M. B. Johnston, L. M. Herz, *Nano Lett.* **2016**, *16*, 7001.

[27] G. Grancini, C. Roldán-Carmona, I. Zimmermann, E. Mosconi, X. Lee, D. Martineau, S. Narbey, F. Oswald, F. De Angelis, M. Graetzel, M. K. Nazeeruddin, *Nat. Commun.* **2017**, *8*, 15684.

[28] Z. Wang, Q. Lin, F. P. Chmiel, N. Sakai, L. M. Herz, H. J. Snaith, *Nat. Energy* **2017**, *2*, 17135.

[29] Y. Hu, J. Schlipf, M. Wussler, M. L. Petrus, W. Jaegermann, T. Bein, P. Müller-Buschbaum, P. Docampo, *ACS Nano* **2016**, *10*, 5999.

[30] M. Yuan, L. N. Quan, R. Comin, G. Walters, R. Sabatini, O. Voznyy, S. Hoogland, Y. Zhao, E. M. Beauregard, P. Kanjanaboos, Z. Lu, D. H. Kim, E. H. Sargent, *Nat. Nanotechnol.* **2016**, *11*, 872.

[31] P. Li, Y. Zhang, C. Liang, G. Xing, X. Liu, F. Li, X. Liu, X. Hu, G. Shao, Y. Song, *Adv. Mater.* **2018**, *30*, 1805323.

[32] C. L. Davies, J. B. Patel, C. Q. Xia, L. M. Herz, M. B. Johnston, *J. Infrared, Millimeter, Terahertz Waves* **2018**, *39*, 1236.

[33] L. Huang, W. R. L. Lambrecht, *Phys. Rev. B* **2013**, *88*, 165203.

[34] J. M. Frost, K. T. Butler, F. Brivio, C. H. Hendon, M. van Schilfgaarde, A. Walsh, *Nano Lett.* **2014**, *14*, 2584.

[35] E. T. Hoke, D. J. Slotcavage, E. R. Dohner, A. R. Bowring, H. I. Karunadasa, M. D. McGehee, *Chem. Sci.* **2015**, *6*, 613.

[36] W. Rehman, D. P. Mcmeekin, J. B. Patel, R. L. Milot, M. B. Johnston, H. J. Snaith, L. M. Herz, *Energy Environ. Sci.* **2017**, *10*, 361.

[37] M. Hu, C. Bi, Y. Yuan, Y. Bai, J. Huang, *Adv. Sci.* **2016**, *3*, 1500301.

[38] W. Rehman, R. L. Milot, G. E. Eperon, C. Wehrenfennig, J. L. Boland, H. J. Snaith, M. B. Johnston, L. M. Herz, *Adv. Mater.* **2015**, *27*, 7938.

[39] J. S. Yun, J. Seidel, J. Kim, A. M. Soufiani, S. Huang, J. Lau, N. J. Jeon, S. Il Seok, M. A. Green, A. Ho-Baillie, *Adv. Energy Mater.* **2016**, *6*, 1600330.

[40] Y. Shao, Y. Fang, T. Li, Q. Wang, Q. Dong, Y. Deng, Y. Yuan, H. Wei, M. Wang, A. Gruverman, J. Shield, J. Huang, *Energy Environ. Sci.* **2016**, *9*, 1752.

[41] C. Wehrenfennig, M. Liu, H. J. Snaith, M. B. Johnston, L. M. Herz, *Energy Environ. Sci.* **2014**, *7*, 2269.

[42] S. D. Stranks, G. E. Eperon, G. Grancini, C. Menelaou, M. J. P. Alcocer, T. Leijtens, L. M. Herz, A. Petrozza, H. J. Snaith, *Science* **2013**, *342*, 341.

[43] L. M. Herz, *Annu. Rev. Phys. Chem.* **2016**, *67*, 65.

[44] J. M. Richter, M. Abdi-Jalebi, A. Sadhanala, M. Tabachnyk, J. P. H. Rivett, L. M. Pazos-Outón, K. C. Gödel, M. Price, F. Deschler, R. H. Friend, *Nat. Commun.* **2016**, *7*, 13941.

[45] E. S. Parrott, R. L. Milot, T. Stergiopoulos, H. J. Snaith, M. B. Johnston, L. M. Herz, *J. Phys. Chem. Lett.* **2016**, *7*, 1321.

[46] R. L. Milot, G. E. Eperon, H. J. Snaith, M. B. Johnston, L. M. Herz, *Adv. Funct. Mater.* **2015**, *25*, 6218.

[47] N. K. Noel, A. Abate, S. D. Stranks, E. S. Parrott, V. M. Burlakov, A. Goriely, H. J. Snaith, *ACS Nano* **2014**, *8*, 9815.

[48] L. M. Herz, *J. Phys. Chem. Lett.* **2018**, *9*, 6853.

[49] M. B. Johnston, L. M. Herz, *Acc. Chem. Res.* **2016**, *49*, 146.

[50] C. L. Davies, M. R. Filip, J. B. Patel, T. W. Crothers, C. Verdi, A. D. Wright, R. L. Milot, F. Giustino, M. B. Johnston, L. M. Herz, *Nat. Commun.* **2018**, *9*, 293.

[51] T. W. Crothers, R. L. Milot, J. B. Patel, E. S. Parrott, J. Schlipf, P. Müller-Buschbaum, M. B. Johnston, L. M. Herz, *Nano Lett.* **2017**, *17*, 5782.

[52] M. C. Gélvez-Rueda, E. M. Hutter, D. H. Cao, N. Renaud, C. C. Stoumpos, J. T. Hupp, T. J. Savenije, M. G. Kanatzidis, F. C. Grozema, *J. Phys. Chem. C* **2017**, *121*, 26566.